nature physics

LETTERS

PUBLISHED ONLINE: 4 JANUARY 2016 | DOI: 10.1038/NPHYS3607

Ferromagnetic and antiferromagnetic order in bacterial vortex lattices

Hugo Wioland[1,2†], Francis G. Woodhouse[1,3†], Jörn Dunkel[4] and Raymond E. Goldstein[1*]

Despite their inherently non-equilibrium nature[1], living systems can self-organize in highly ordered collective states[2,3] that share striking similarities with the thermodynamic equilibrium phases[4,5] of conventional condensed-matter and fluid systems. Examples range from the liquid-crystal-like arrangements of bacterial colonies[6,7], microbial suspensions[8,9] and tissues[10] to the coherent macro-scale dynamics in schools of fish[11] and flocks of birds[12]. Yet, the generic mathematical principles that govern the emergence of structure in such artificial[13] and biological[6–9,14] systems are elusive. It is not clear when, or even whether, well-established theoretical concepts describing universal thermostatistics of equilibrium systems can capture and classify ordered states of living matter. Here, we connect these two previously disparate regimes: through microfluidic experiments and mathematical modelling, we demonstrate that lattices of hydrodynamically coupled bacterial vortices can spontaneously organize into distinct patterns characterized by ferro- and antiferromagnetic order. The coupling between adjacent vortices can be controlled by tuning the inter-cavity gap widths. The emergence of opposing order regimes is tightly linked to the existence of geometry-induced edge currents[15,16], reminiscent of those in quantum systems[17–19]. Our experimental observations can be rationalized in terms of a generic lattice field theory, suggesting that bacterial spin networks belong to the same universality class as a wide range of equilibrium systems.

Lattice field theories (LFTs) have been instrumental in uncovering a wide range of fundamental physical phenomena, from quark confinement in atomic nuclei[20] and neutron stars[21] to topologically protected states of matter[22] and transport in novel magnetic[23] and electronic[24,25] materials. LFTs can be constructed either by discretizing the spacetime continuum underlying classical and quantum field theories[20], or by approximating discrete physical quantities, such as the electron spins in a crystal lattice, through continuous variables. In equilibrium thermodynamics, LFT approaches have proved invaluable both computationally and analytically, for a single LFT often represents a broad class of microscopically distinct physical systems that exhibit the same universal scaling behaviours in the vicinity of a phase transition[4,26]. However, until now there has been little evidence as to whether the emergence of order in living matter can be understood within this universality framework. Our combined experimental and theoretical analysis reveals a number of striking analogies between the collective cell dynamics in bacterial fluids and known phases of condensed-matter systems, thereby implying that universality concepts may be more broadly applicable than previously thought.

To realize a microbial non-equilibrium LFT, we injected dense suspensions of the rod-like swimming bacterium *Bacillus subtilis* into shallow polydimethyl siloxane (PDMS) chambers in which identical circular cavities are connected to form one- and two-dimensional (2D) lattice networks (Fig. 1, Supplementary Fig. 6 and Methods). Each cavity is 50 μm in diameter and 18 μm deep, a geometry known to induce a stably circulating vortex when a dense bacterial suspension is confined within an isolated flattened droplet[15]. For each cavity i, we define the continuous vortex spin variable $V_i(t)$ at time t as the total angular momentum of the local bacterial flow within this cavity, determined by particle imaging velocimetry (PIV) analysis (Fig. 1b,f; Supplementary Movies 1 and 2 and Methods). To account for the effect of oxygenation variability on suspension motility[9], flow velocities are normalized by the overall root-mean-square (r.m.s.) speed measured in the corresponding experiment. Bacterial vortices in neighbouring cavities interact through a gap of predetermined width w (Fig. 1f). To explore different interaction strengths, we performed experiments over a range of gap parameters w (Methods). For square lattices, we varied w from 4 to 25 μm and found that for all but the largest gaps, $w \leq w_* \approx 20\,\mu\text{m}$, the suspensions generally self-organize into coherent vortex lattices, exhibiting domains of correlated spins whose characteristics depend on coupling strength (Fig. 1a,e). If the gap size exceeds w_*, bacteria can move freely between cavities and individual vortices cease to exist. Here, we focus exclusively on the vortex regime $w < w_*$ and quantify preferred magnetic order through the normalized mean spin–spin correlation $\chi = \langle \Sigma_{i\sim j} V_i(t) V_j(t) / \Sigma_{i\sim j} |V_i(t) V_j(t)| \rangle$, where $\Sigma_{i\sim j}$ denotes a sum over pairs $\{i,j\}$ of adjacent cavities and $\langle \cdot \rangle$ denotes time average.

Square lattices reveal two distinct states of preferred magnetic order (Fig. 1a,e,i), one with $\chi < 0$ and the other with $\chi > 0$, transitioning between them at a critical gap width $w_{\text{crit}} \approx 8\,\mu\text{m}$ (Fig. 1j). For subcritical values $w < w_{\text{crit}}$, we observe an antiferromagnetic phase with anti-correlated ($\chi < 0$) spin orientations between neighbouring chambers on average (Fig. 1a and Supplementary Movie 1). By contrast, for $w > w_{\text{crit}}$, spins are positively correlated ($\chi > 0$) in a ferromagnetic phase (Fig. 1e and Supplementary Movie 2). Noting that the r.m.s. spin $\langle V_i(t)^2 \rangle^{1/2}$ decays only slowly with increasing gap width $w \to w_*$ (Fig. 1k), and that the chambers do not impose any preferred handedness

[1]Department of Applied Mathematics and Theoretical Physics, University of Cambridge, Wilberforce Road, Cambridge CB3 0WB, UK. [2]Institut Jacques Monod, Centre Nationale pour la Recherche Scientifique (CNRS), UMR 7592, Université Paris Diderot, Sorbonne Paris Cité, F-75205 Paris, France. [3]Faculty of Engineering, Computing and Mathematics, The University of Western Australia, 35 Stirling Highway, Crawley, Perth, Western Australia 6009, Australia. [4]Department of Mathematics, Massachusetts Institute of Technology, 77 Massachusetts Avenue, Cambridge, Massachusetts 02139-4307, USA. †Present addresses: Institut Jacques Monod, Centre Nationale pour la Recherche Scientifique (CNRS), UMR 7592, Université Paris Diderot, Sorbonne Paris Cité, F-75205 Paris, France (H.W.); Department of Applied Mathematics and Theoretical Physics, University of Cambridge, Wilberforce Road, Cambridge CB3 0WB, UK (F.G.W.). *e-mail: R.E.Goldstein@damtp.cam.ac.uk

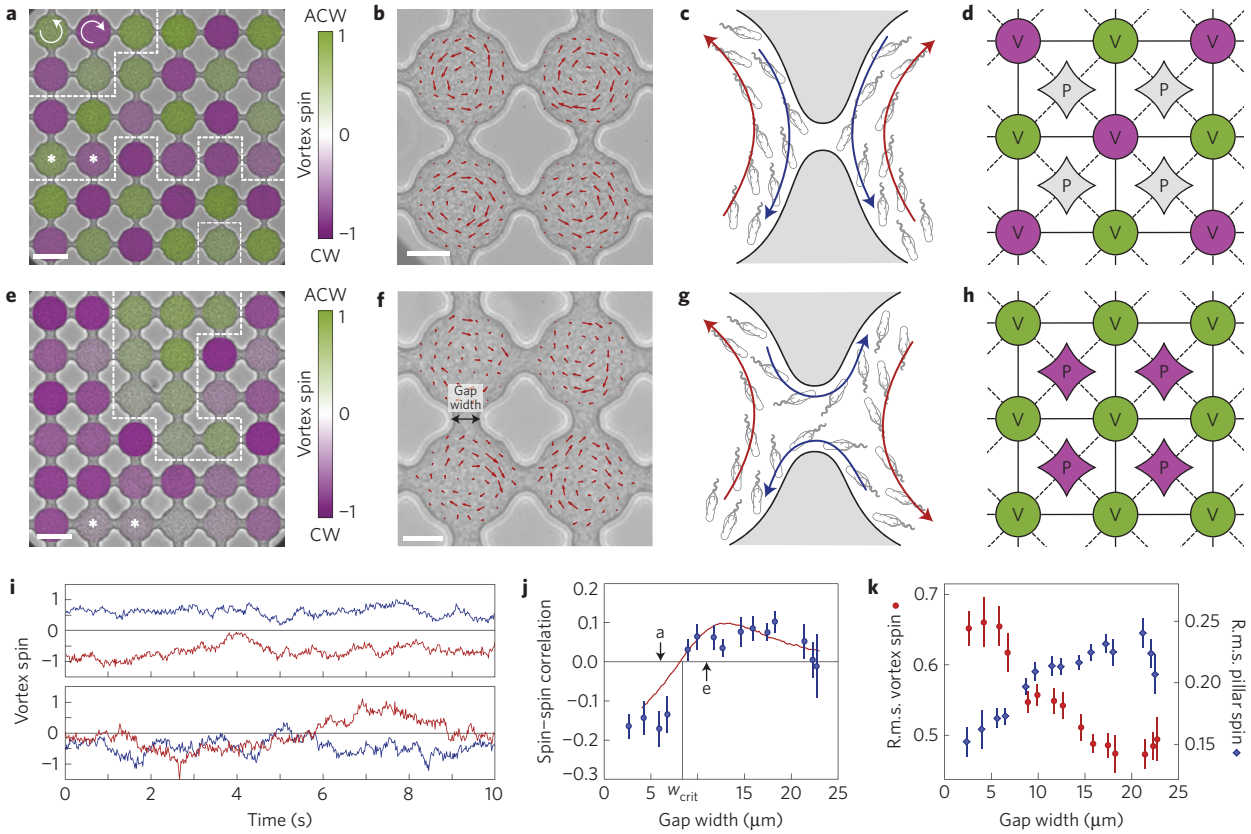

Figure 1 | Edge currents determine antiferromagnetic and ferromagnetic order in a square lattice of bacterial vortices. a, Three domains of antiferromagnetic order highlighted by dashed white lines (gap width $w = 6\,\mu m$). Scale bar, 50 μm. Overlaid false colour shows spin magnitude (see Supplementary Movie 1 for raw data). **b**, Bacterial flow PIV field within an antiferromagnetic domain (Supplementary Movie 1). For clarity, not all velocity vectors are shown. Largest arrows correspond to speed $40\,\mu m\,s^{-1}$. Scale bar, 20 μm. **c**, Schematic of bacterial flow circulation in the vicinity of a gap. For small gaps $w < w_{crit}$, bacteria forming the edge currents (blue arrows) swim across the gap, remaining in their original cavity. Bulk flow (red) is directed opposite to the edge current[15,16] (Supplementary Movie 3). **d**, Graph of the Union Jack double-lattice model in an antiferromagnetic state with zero net pillar circulation. Solid and dashed lines depict vortex–vortex and vortex–pillar interactions of respective strengths J_v and J_p. Vortices and pillars are colour-coded according to their spin. **e**, For supercritical gap widths $w > w_{crit}$, extended domains of ferromagnetic order predominate (Supplementary Movie 2; $w = 11\,\mu m$). Scale bar, 50 μm. **f**, PIV field within a ferromagnetic domain (Supplementary Movie 2). Largest arrows: $36\,\mu m\,s^{-1}$. Scale bar, 20 μm. **g**, For $w > w_{crit}$, bacteria forming the edge current (blue arrows) swim along the PDMS boundary through the gap, driving bulk flows (red) in the opposite directions, thereby aligning neighbouring vortex spins. **h**, Ferromagnetic state of the Union Jack lattice induced by edge current loops around the pillars. **i**, Trajectories of neighbouring spins (∗-symbols in **a**,**e**) fluctuate over time, signalling exploration of a fluctuating steady state under a non-zero effective temperature (top, antiferromagnetic; bottom, ferromagnetic). **j**, The zero of the spin–spin correlation χ at $w_{crit} \approx 8\,\mu m$ marks the phase transition. The best-fit Union Jack model (solid line) is consistent with the experimental data. **k**, R.m.s. vortex spin $\langle V_i^2 \rangle^{1/2}$ decreases with the gap size w, showing weakening of the circulation. R.m.s. pillar spin $\langle P_j^2 \rangle^{1/2}$ increases with w, reflecting enhanced bacterial circulation around pillars. Each point in **j**,**k** represents an average over ≥5 movies in 3 μm bins at 1.5 μm intervals; vertical bars indicate standard errors (Methods).

on the vortex spins (Supplementary Fig. 1 and Supplementary Section 1), we conclude that the observed phase behaviour is caused by spin–spin interactions. However, although both phases possess a well-defined average vortex–vortex correlation, the individual spins fluctuate randomly over time as ordered domains split, merge and flip (Fig. 1i and Supplementary Figs 1 and 3) while the system explores configuration space inside a statistical steady state (Supplementary Sections 1 and 3). Thus, although the bacterial vortex spins $\{V_i(t)\}$ define a real-valued lattice field, the phenomenology of these continuous bacterial spin lattices is qualitatively similar to that of the classical 2D Ising model[4] with discrete binary spin variables $s_i \in \{\pm 1\}$, whose configurational probability at finite temperature $T = (k_B\beta)^{-1}$ is described by a thermal Boltzmann distribution $\propto \exp(-\beta J \Sigma_{i\sim j} s_i s_j)$, where $J > 0$ corresponds to ferromagnetic and $J < 0$ to antiferromagnetic order. The detailed theoretical analysis below shows that the observed phases in the bacterial spin system can be understood quantitatively in terms of a generic quartic LFT comprising two dual interacting lattices. The introduction of a double lattice is necessitated by the microscopic structure of the underlying bacterial flows. By analogy with a lattice of interlocking cogs, one might have intuitively expected that the antiferromagnetic phase would generally be favoured, because only in this configuration does the bacterial flow along the cavity boundaries conform across the inter-cavity gap, avoiding the potentially destabilizing head-to-head collisions that would occur with opposing flows (Fig. 1b,c). However, the extent of the observed ferromagnetic phase highlights a competing biofluid-mechanical effect.

Just as the quantum Hall effect[17] and the transport properties of graphene[18,19] arise from electric edge currents, the opposing order regimes observed here are explained by the existence of analogous bacterial edge currents. At the boundary of an isolated flattened droplet of a bacterial suspension, a single layer of cells—an edge current—can be observed swimming against the bulk circulation[15,16]. This narrow cell layer is key to the suspension dynamics: the hydrodynamics of the edge current circulating

in one direction advects nearby cells in the opposite direction, which in turn dictate the bulk circulation by flow continuity through steric and hydrodynamic interactions[16,27]. Identical edge currents are present in our lattices (Supplementary Movie 3) and explain both order regimes as follows. In the antiferromagnetic regime, when $w < w_{crit}$, the bacterial edge current driving a particular vortex will pass over the gap without leaving the cavity (Fig. 1c). Interaction with a neighbouring edge current through the gap favours parallel flow, inducing counter-circulation of neighbouring vortices and therefore driving antiferromagnetic order (Fig. 1d). However, when $w > w_{crit}$, the edge currents can no longer pass over the gaps and instead wind around the star-shaped pillars dividing the cavities (Fig. 1g). A clockwise (resp. anticlockwise) bacterial edge current about a pillar induces anticlockwise (resp. clockwise) fluid circulation about the pillar in a thin region near its boundary. Flow continuity then induces clockwise (resp. anticlockwise) flow in all cavities adjacent to the pillar, resulting in ferromagnetic order (Fig. 1h). Thus by viewing the system as an anti-cooperative Union Jack lattice[28,29] of both bulk vortex spins V_i and near-pillar circulations P_j, we accommodate both order regimes: antiferromagnetism as indefinite circulations $P_j = 0$ and alternating spins $V_i = \pm V$ (Fig. 1d), and ferromagnetism as definite circulations $P_j = -P < 0$ and uniform spins $V_i = V > 0$ (Fig. 1h). To verify these considerations, we determined the net near-pillar circulation $P_j(t)$ using PIV (Methods) and found that the r.m.s. circulation $\langle P_j(t)^2\rangle^{1/2}$ shows the expected monotonic increase as the inter-cavity gap widens (Fig. 1k).

Competition between the vortex–vortex and vortex–pillar interactions determines the resultant order regime. Their relative strengths can be inferred by mapping each experiment onto a continuous-spin Union Jack lattice (Fig. 1d,h). In this model, the interaction energy of the time-dependent vortex spins $\mathbf{V} = \{V_i\}$ and pillar circulations $\mathbf{P} = \{P_j\}$ is defined by the LFT Hamiltonian

$$H(\mathbf{V},\mathbf{P}) = -J_v \sum_{V_i \sim V_j} V_i V_j - J_p \sum_{V_i \sim P_j} V_i P_j + \sum_{V_i} \left(\frac{1}{2} a_v V_i^2 + \frac{1}{4} b_v V_i^4 \right) + \sum_{P_j} \frac{1}{2} a_p P_j^2 \qquad (1)$$

The first two sums are vortex–vortex and vortex–pillar interactions with strengths $J_v, J_p < 0$, where $\sim$ denotes adjacent lattice pairs. The last two sums are individual vortex and pillar circulation potentials. Vortices must be subject to a quartic potential function with $b_v > 0$ to allow for a potentially double-welled potential if $a_v < 0$, encoding the observed symmetry breaking into spontaneous circulation in the absence of other interactions[15,27]. In contrast, our data analysis implies that pillar circulations are sufficiently described by a quadratic potential of strength $a_p > 0$ (Supplementary Fig. 4 and Supplementary Section 4). To account for the experimentally observed spin fluctuations (Fig. 1i and Supplementary Fig. 1), we model the dynamics of the lattice fields $\mathbf{V}$ and $\mathbf{P}$ through the coupled stochastic differential equations (SDEs)

$$d\mathbf{V} = -(\partial H/\partial \mathbf{V})\, dt + \sqrt{2T_v}\, d\mathbf{W}_v \qquad (2)$$

$$d\mathbf{P} = -(\partial H/\partial \mathbf{P})\, dt + \sqrt{2T_p}\, d\mathbf{W}_p \qquad (3)$$

where $\mathbf{W}_v$ and $\mathbf{W}_p$ are vectors of uncorrelated Wiener processes representing intrinsic and thermal fluctuations. The overdamped dynamics in equations (2) and (3) neglects dissipative Onsager-type cross-couplings, as the dominant contribution to friction stems from the nearby no-slip PDMS boundaries (Supplementary Section 7). The parameters T_v and T_p set the strength of random perturbations from energy-minimizing behaviour. In the equilibrium limit when $T_v = T_p = T$, the stationary statistics of the solutions of equations (2) and (3) obey the Boltzmann distribution $\propto e^{-H/T}$. We inferred all seven parameters of the full SDE model for each experiment by linear regression on a discretization of the SDEs (Supplementary Fig. 2 and Supplementary Section 2). The differing sublattice temperatures $T_v \neq T_p$ found show that the system is not in thermodynamic equilibrium owing to its active microscopic constituents (Supplementary Fig. 2). Instead, the system is in a pseudo-equilibrium statistical steady state (Supplementary Section 1), which we will soon show can be reduced to an equilibrium-like description. As a cross-validation, we fitted appropriate functions of gap width w to these estimates and simulated the resulting SDE model over a range of w on a 6×6 lattice concordant with the observations (Supplementary Section 3). The agreement between experimental data and the numerically obtained vortex–vortex correlation $\chi(w)$ supports the validity of the double-lattice model and its underlying approximations (Fig. 1j).

To reconnect with the classical 2D Ising model and understand better the experimentally observed phase transition, we project the Hamiltonian (1) onto an effective square lattice model by making a mean-field assumption for the pillar circulations. In the experiments, P_i is linearly correlated with the average spin of its vortex neighbours $[P_i]_V = (1/4)\Sigma_{j:V_j \sim P_i} V_j$, with a constant of proportionality $-\alpha < 0$ only weakly dependent on gap width (Supplementary Fig. 4 and Supplementary Section 4). Replacing effectively $P_i \to -\alpha[P_i]_V$ as a mean-field variable in the model eliminates all pillar circulations, yielding a standard quartic LFT for $\mathbf{V}$ (see Supplementary Section 4 for a detailed derivation). The mean-field dynamics are then governed by the reduced SDE $d\mathbf{V} = -(\partial \hat{H}/\partial \mathbf{V})\, dt + \sqrt{2T}\, d\mathbf{W}$ with effective temperature $T \approx T_v + 4T_p J_p^2/a_p^2$ and energy

$$\hat{H}(\mathbf{V}) = -J \sum_{V_i \sim V_j} V_i V_j + \sum_{V_i} \left(\frac{1}{2} a V_i^2 + \frac{1}{4} b V_i^4 \right)$$

which has steady-state probability density $p(\mathbf{V}) \propto e^{-\beta \hat{H}}$ with $\beta = 1/T$, and where $a = a_v - 4J_p^2/a_p$ and $b = b_v$. Note that in the limit $a \to -\infty$ and $b \to +\infty$ with a/b fixed, the classical two-state Ising model is recovered by identifying $s_i = V_i/\sqrt{|a|/b} \in \{\pm 1\}$. The reduced coupling constant J relates to those of the double-lattice model (J_v, J_p) in the thermodynamic limit as $J \approx J_v - (1/2)\alpha J_p$ (Supplementary Section 4), making manifest how competition between J_v and J_p can result in both antiferromagnetic $(|J_v| > (1/2)\alpha|J_p|)$ or ferromagnetic $(|J_v| < (1/2)\alpha|J_p|)$ behaviour. We estimated βJ, βa and βb for each experiment by directly fitting the effective one-spin potential $\mathcal{V}^{\text{eff}}(V\,|\,[V]_V) = -4\beta J V[V]_V + (1/2)\beta a V^2 + (1/4)\beta b V^4$ via the log-likelihood $\log p(V\,|\,[V]_V) = -\mathcal{V}^{\text{eff}} + \text{const}$ (Fig. 2, Supplementary Fig. 5 and Supplementary Section 5). These estimates match those obtained independently using SDE regression methods (Fig. 2a–c and Supplementary Section 5), and show the transition from antiferromagnetic interaction ($\beta J < 0$) to ferromagnetic interaction ($\beta J > 0$) at w_{crit} (Fig. 2a). As the gap width increases, the energy barrier to spin change falls (Fig. 2b) and the magnitude of the lowest energy spin decreases (Fig. 2c) as a result of weakening confinement within each cavity, visible as a flattening of the one-spin effective potential $\mathcal{V}^{\text{eff}}$ (Fig. 2d–f and Supplementary Fig. 5).

Experiments on lattices of different symmetry groups lend further insight into the competition between edge currents and bulk flow. Unlike their square counterparts, triangular lattices cannot support antiferromagnetic states without frustration. Therefore, ferromagnetic order should be enhanced in a triangular bacterial spin lattice. This is indeed observed in our experiments: at moderate gap size $w \lesssim 18\,\mu m$, we found exclusively a highly

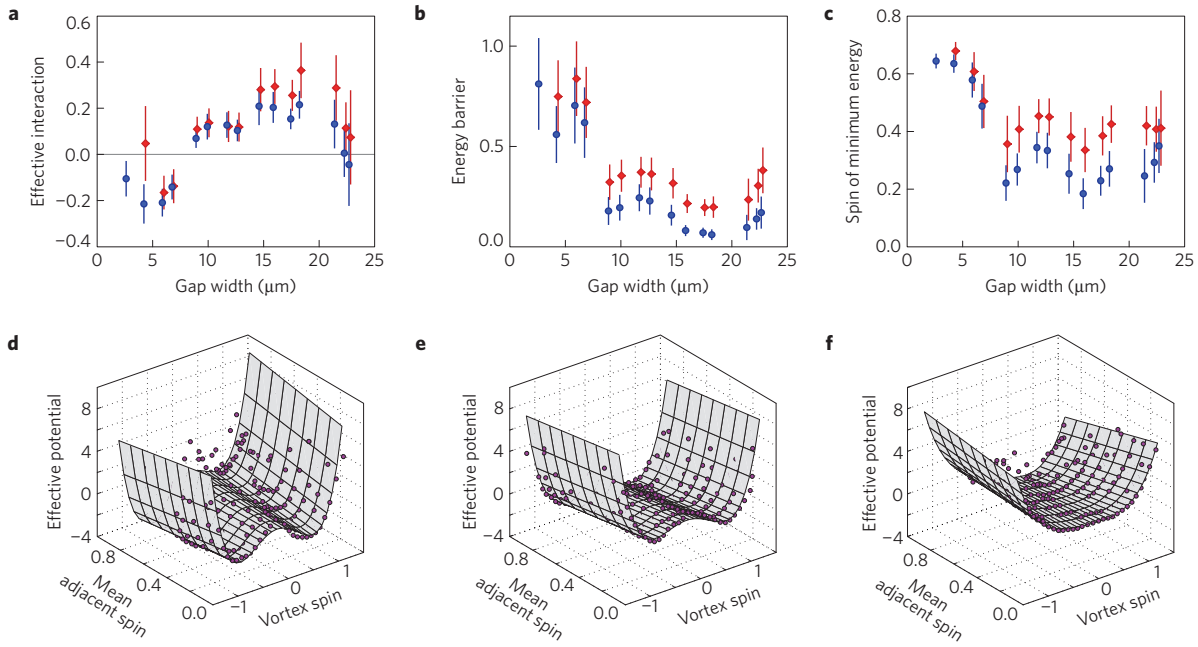

Figure 2 | Best-fit mean-field LFT model captures the phase transition in the square lattice. a, A sign change of the effective interaction βJ signals the transition from antiferro- to ferromagnetic states. **b**, The effective energy barrier, $\beta a^2/(4b)$ when $a<0$ and zero when $a>0$ (Supplementary Section 5), decreases with the gap size w, reflecting increased susceptibility to fluctuations. **c**, The spin $V_{\min}$ minimizing the single-spin potential (Supplementary Section 5) decreases with w in agreement with the decrease in the r.m.s. vortex spin (Fig. 1k). Each point in **a**–**c** represents an average over ≥5 movies in 3 μm bins at 1.5 μm intervals; blue circles are from distribution fitting, red diamonds are from SDE regression, and vertical bars indicate standard errors (Methods). **d**–**f**, Examples of the effective single-spin potential $\mathcal{V}^{\text{eff}}$ conditional on the mean spin of adjacent vortices $[V]_V$. Data (points) and estimated potential (surface) for three movies with gap widths 6, 10 and 17 μm.

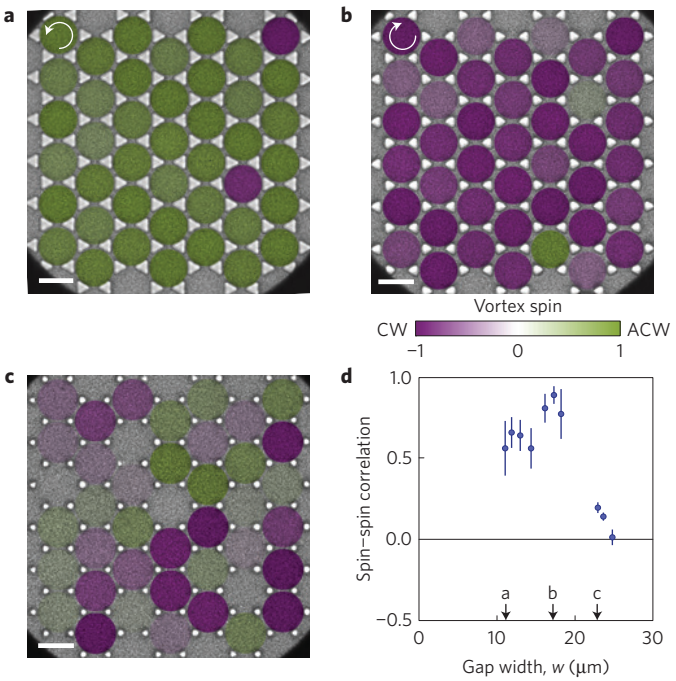

Figure 3 | Frustration in triangular lattices determines the preferred order. **a**,**b**, Triangular lattices favour ferromagnetic states of either handedness (Supplementary Movie 4). Vortices are colour-coded by spin. **c**, At the largest gap size, bacterial circulation becomes unstable. Scale bar, 50 μm. **d**, The spin–spin correlation χ shows strongly enhanced ferromagnetic order compared with the square lattice (Fig. 1j). Each point represents an average over ≥5 movies in 3 μm bins at 1.5 μm intervals; vertical bars indicate standard errors (Methods).

robust ferromagnetic phase of either handedness (Fig. 3a,b,d and Supplementary Movie 4), reminiscent of quantum vortex lattices in Bose–Einstein condensates[30]. At comparable gap size, the spin correlation is approximately four to eight times larger than in the square lattice. Increasing the gap size beyond 20 μm eventually destroys the spontaneous circulation within the cavities and a disordered state prevails (Fig. 3c,d), with a sharper transition than for the square lattices (Fig. 1j). Conversely, a 1D line lattice exclusively exhibits antiferromagnetic order as the suspension is unable to maintain the very long uniform edge currents that would be necessary to sustain a ferromagnetic state (Supplementary Fig. 6 and Supplementary Section 6). These results manifest the importance of lattice geometry and dimensionality for vortex ordering in bacterial spin lattices, in close analogy with their electromagnetic counterparts.

Understanding the ordering principles of microbial matter is a key challenge in active materials design[13], quantitative biology and biomedical research. Improved prevention strategies for pathogenic biofilm formation, for example, will require detailed knowledge of how bacterial flows interact with complex porous surface structures to create the stagnation points at which biofilms can nucleate. Our study shows that collective excitations in geometrically confined bacterial suspensions can spontaneously organize in phases of magnetic order that can be robustly controlled by edge currents. These results demonstrate fundamental similarities with a broad class of widely studied quantum systems[17,19,30], suggesting that theoretical concepts originally developed to describe magnetism in disordered media could potentially capture microbial behaviours in complex environments. Future studies may try to explore further the range and limits of this promising analogy.

Methods

Methods and any associated references are available in the online version of the paper.

Received 11 June 2015; accepted 13 November 2015; published online 4 January 2016

References

1. Schrödinger, E. *What is Life?* (Cambridge Univ. Press, 1944).
2. Vicsek, T. & Zafeiris, A. Collective motion. *Phys. Rep.* **517**, 71–140 (2012).
3. Marchetti, M. C. *et al*. Hydrodynamics of soft active matter. *Rev. Mod. Phys.* **85**, 1143–1189 (2013).
4. Kardar, M. *Statistical Physics of Fields* (Cambridge Univ. Press, 2007).
5. Mermin, N. D. The topological theory of defects in ordered media. *Rev. Mod. Phys.* **51**, 591–648 (1979).
6. Ben Jacob, E., Becker, I., Shapira, Y. & Levine, H. Bacterial linguistic communication and social intelligence. *Trends Microbiol.* **12**, 366–372 (2004).
7. Volfson, D., Cookson, S., Hasty, J. & Tsimring, L. S. Biomechanical ordering of dense cell populations. *Proc. Natl Acad. Sci. USA* **150**, 15346–15351 (2008).
8. Riedel, I. H., Kruse, K. & Howard, J. A self-organized vortex array of hydrodynamically entrained sperm cells. *Science* **309**, 300–303 (2005).
9. Dunkel, J. *et al*. Fluid dynamics of bacterial turbulence. *Phys. Rev. Lett.* **110**, 228102 (2013).
10. Wu, J., Roman, A.-C., Carvajal-Gonzalez, J. M. & Mlodzik, M. Wg and Wnt4 provide long-range directional input to planar cell polarity orientation in drosophila. *Nature Cell Biol.* **15**, 1045–1055 (2013).
11. Katz, Y., Ioannou, C. C., Tunstro, K., Huepe, C. & Couzin, I. D. Inferring the structure and dynamics of interactions in schooling fish. *Proc. Natl Acad. Sci. USA* **108**, 18720–18725 (2011).
12. Cavagna, A. *et al*. Scale-free correlations in starling flocks. *Proc. Natl Acad. Sci. USA* **107**, 11865–11870 (2010).
13. Sanchez, T., Chen, D. T. N., DeCamp, S. J., Heymann, M. & Dogic, Z. Spontaneous motion in hierarchically assembled active matter. *Nature* **491**, 431–434 (2012).
14. Sokolov, A. & Aranson, I. S. Physical properties of collective motion in suspensions of bacteria. *Phys. Rev. Lett.* **109**, 248109 (2012).
15. Wioland, H., Woodhouse, F. G., Dunkel, J., Kessler, J. O. & Goldstein, R. E. Confinement stabilizes a bacterial suspension into a spiral vortex. *Phys. Rev. Lett.* **110**, 268102 (2013).
16. Lushi, E., Wioland, H. & Goldstein, R. E. Fluid flows created by swimming bacteria drive self-organization in confined suspensions. *Proc. Natl Acad. Sci. USA* **111**, 9733–9738 (2014).
17. Büttiker, M. Absence of backscattering in the quantum Hall effect in multiprobe conductors. *Phys. Rev. B* **38**, 9375–9389 (1988).
18. Kane, C. L. & Mele, E. J. Quantum spin Hall effect in graphene. *Phys. Rev. Lett.* **95**, 226801 (2005).
19. Castro Neto, A. H., Guinea, F., Peres, N. M. R., Novoselov, K. S. & Geim, A. K. The electronic properties of graphene. *Rev. Mod. Phys.* **81**, 109–162 (2009).
20. Wilson, K. G. Confinement of quarks. *Phys. Rev. D* **10**, 2445–2459 (1974).
21. Glendenning, N. K. *Compact Stars: Nuclear Physics, Particle Physics, and General Relativity* (Springer, 2000).
22. Battye, R. A. & Sutcliffe, P. M. Skyrmions with massive pions. *Phys. Rev. C* **73**, 055205 (2006).
23. Nagaosa, N. & Tokura, Y. Topological properties and dynamics of magnetic skyrmions. *Nature Nanotech.* **8**, 899–911 (2013).
24. Novoselov, K. S. *et al*. Two-dimensional gas of massless Dirac fermions in graphene. *Nature* **438**, 197–200 (2005).
25. Drut, J. E. & Lähde, T. A. Lattice field theory simulations of graphene. *Phys. Rev. B* **79**, 165425 (2009).
26. Fernández, R., Fröhlich, J. & Sokal, A. D. *Random Walks, Critical Phenomena, and Triviality in Quantum Field Theory* (Springer, 1992).
27. Woodhouse, F. G. & Goldstein, R. E. Spontaneous circulation of confined active suspensions. *Phys. Rev. Lett.* **109**, 168105 (2012).
28. Vaks, V. G., Larkin, A. I. & Ovchinnikov, Y. N. Ising model with interaction between non-nearest neighbors. *Sov. Phys. JETP* **22**, 820–826 (1966).
29. Stephenson, J. Ising model with antiferromagnetic next-nearest-neighbor coupling: spin correlations and disorder points. *Phys. Rev. B* **1**, 4405–4409 (1970).
30. Abo-Shaeer, J. R., Raman, C., Vogels, J. M. & Ketterle, W. Observation of vortex lattices in Bose–Einstein condensates. *Science* **292**, 476–479 (2001).

Acknowledgements

We thank V. Kantsler and E. Lushi for assistance and discussions. This work was supported by European Research Council Advanced Investigator Grant 247333 (H.W. and R.E.G.), EPSRC (H.W. and R.E.G.), an MIT Solomon Buchsbaum Fund Award (J.D.) and an Alfred P. Sloan Research Fellowship (J.D.).

Author contributions

All authors designed the research and collaborated on theory. H.W. performed experiments and PIV analysis. H.W. and F.G.W. analysed PIV data and performed parameter inference. F.G.W. and J.D. wrote simulation code. All authors wrote the paper.

Additional information

Supplementary information is available in the online version of the paper. Reprints and permissions information is available online at www.nature.com/reprints. Correspondence and requests for materials should be addressed to R.E.G.

Competing financial interests

The authors declare no competing financial interests.

Methods

Experiments. Wild-type *Bacillus subtilis* cells (strain 168) were grown in Terrific Broth (Sigma). A monoclonal colony was transferred from an agar plate to 25 ml of medium and left to grow overnight at 35 °C on a shaker. The culture was diluted 200-fold into fresh medium and harvested after approximately 5 h, when more than 90% of the bacteria were swimming, as visually verified on a microscope. 10 ml of the suspension was then concentrated by centrifugation at 1,500*g* for 10 min, resulting in a pellet with volume fraction approximately 20% which was used without further dilution.

The microchambers were made of polydimethyl siloxane (PDMS) bound to a glass coverslip by oxygen plasma etching. These comprised a square, triangular or linear lattice of ∼18-μm-deep circular cavities with 60 μm between centres, each of diameter ∼50 μm, connected by 4–25-μm-wide gaps for linear and square lattices (Fig. 1a,e and Supplementary Fig. 6) and 10–25-μm-wide gaps for triangular lattices (Fig. 3a–c). The smallest possible gap size was limited by the fidelity of the etching.

Approximately 5 μl of the concentrated suspension was manually injected into the chamber using a syringe. Both inlets were then sealed to prevent external flow. We imaged the suspension on an inverted microscope (Zeiss, Axio Observer Z1) under bright-field illumination, through a 40× oil-immersion objective. Movies 10 s in length were recorded at 60 f.p.s. on a high-speed camera (Photron Fastcam SA3) at 4 and 8 min after injection. Although the PDMS lattices were typically ∼15 cavities across, to avoid boundary effects and to attain the pixel density necessary for PIV we imaged a central subregion spanning 6 × 6 cavities for square lattices, 7 × 6 cavities for triangular lattices, and 7 cavities for linear lattices (multiple of which were captured on a single slide).

Fluorescence in Supplementary Movie 3 was achieved by labelling the membranes of a cell subpopulation with fluorophore FM4-64 following the protocol of Lushi *et al.*[16] The suspension was injected into an identical triangular lattice as in the primary experiments and imaged at 5.6 f.p.s. on a spinning-disc confocal microscope through a 63× oil-immersion objective.

Analysis. For each frame of each movie, the bacterial suspension flow field $\mathbf{u}(x,y,t)$ was measured by standard particle image velocimetry (PIV) without time averaging, using a customized version of mPIV (http://www.oceanwave.jp/softwares/mpiv). PIV subwindows were 16 × 16 pixels with 50% overlap, yielding ∼150 vectors per cavity per frame. Cavity regions were identified in each movie by manually placing the centre and radius of the bottom left cavity, measuring vectors to its immediate neighbours, and repeatedly translating to generate the full grid. Pillar edges were then calculated from the cavity grid and the gap width (measured as the minimum distance between adjacent pillars).

The spin $V_i(t)$ of each cavity i at time t is defined as the normalized planar angular momentum

$$V_i(t) = \frac{\hat{\mathbf{z}} \cdot \left[\sum_{(x,y)_i} \mathbf{r}_i(x,y) \times \mathbf{u}(x,y,t)\right]}{\overline{U} \sum_{(x,y)_i} |\mathbf{r}_i(x,y)|}$$

where $\mathbf{r}_i(x,y)$ is the vector from the cavity centre to (x,y), and sums run over all PIV grid points $(x,y)_i$ inside cavity i. For each movie, we normalize velocities by the root-mean-square (r.m.s.) suspension velocity $\overline{U} = \langle \mathbf{u}(x,y,t)^2 \rangle^{1/2}$, where the average is over all grid points (x,y) and all times t, to account for the effects of variable oxygenation on motility[9]; we found an ensemble average $\mathbb{E}[\bar{U}] = 12.1\,\mu\mathrm{m\,s^{-1}}$ with s.d. $3.6\,\mu\mathrm{m\,s^{-1}}$ over all experiments. This definition has $V_i(t) > 0$ for anticlockwise spin and $V_i(t) < 0$ for clockwise spin. A vortex of radially independent speed—that is, $\mathbf{u}(x,y,t) = u\hat{\boldsymbol{\theta}}$, where $\hat{\boldsymbol{\theta}}$ is the azimuthal unit vector—has $V_i(t) = \pm 1$; conversely, randomly oriented flow has $V_i(t) = 0$. The average spin–spin correlation χ of a movie is then defined as

$$\chi = \left\langle \frac{\sum_{i\sim j} V_i(t) V_j(t)}{\sum_{i\sim j} |V_i(t) V_j(t)|} \right\rangle$$

where $\Sigma_{i\sim j}$ denotes a sum over pairs $\{i,j\}$ of adjacent cavities and $\langle\cdot\rangle$ denotes an average over all frames. If all vortices share the same sign, then $\chi = 1$ (ferromagnetism); if each vortex is of opposite sign to its neighbours, then $\chi = -1$ (antiferromagnetism); if the vortices are uniformly random, then $\chi = 0$. Similarly, the circulation $P_j(t)$ about pillar j at time t is defined as the normalized average tangential velocity

$$P_j(t) = \frac{\sum_{(x,y)_j} \mathbf{u}(x,y,t) \cdot \hat{\mathbf{t}}_j(x,y)}{\overline{U} \sum_{(x,y)_j} 1}$$

where $\hat{\mathbf{t}}_j(x,y)$ is the unit vector tangential to the pillar, and sums run over PIV grid points $(x,y)_j$ closer than 5 μm to the pillar j.

Results presented are typically averaged in bins of fixed gap width. All plots with error bars use 3 μm bins, calculated every 1.5 μm (50% overlap), and bins with fewer than five movies were excluded. Error bars denote standard error. Bin counts for square lattices (Figs 1j,k and 2a–c and Supplementary Figs 4 and 7) are 8, 8, 13, 14, 21, 27, 27, 22, 18, 22, 20, 11, 7, 13, 7; bin counts for triangular lattices (Fig. 3d) are 5, 14, 16, 13, 16, 15, 5, 5, 10, 7; and bin counts for linear lattices (Supplementary Fig. 6) are 5, 7, 8, 8, 9, 9, 6, 5, 6, 7, 6, 8, 9, 5, 6, 5, 6.

nature physics

SUPPLEMENTARY INFORMATION

DOI: 10.1038/NPHYS3607

Ferromagnetic and antiferromagnetic order in bacterial vortex lattices

Hugo Wioland[1,2†], Francis G. Woodhouse[1†,3], Jörn Dunkel[4], and Raymond E. Goldstein[1]

[1]Department of Applied Mathematics and Theoretical Physics, University of Cambridge, Wilberforce Road, Cambridge CB3 0WB, U.K.

[2]Institut Jacques Monod, Centre Nationale pour la Recherche Scientifique (CNRS), UMR 7592, Université Paris Diderot, Sorbonne Paris Cité, F-75205 Paris, France

[3]Faculty of Engineering, Computing and Mathematics, The University of Western Australia, 35 Stirling Highway, Crawley, Perth WA 6009, Australia

[4]Department of Mathematics, Massachusetts Institute of Technology, 77 Massachusetts Avenue, Cambridge MA 02139-4307, U.S.A.

[†]*Present address.*

1 Experimental consistency with theoretical model

In populating our chosen theoretical models, we make important assumptions of the experimental data concerning spin bias, statistical steadiness, and phase-space exploration. In the following, we discuss these assumptions and provide evidence for their validity.

1.1 Absence of spin handedness bias

In the Hamiltonian (1), we assume a symmetric local quartic potential. For this to be valid, the vortices must be free of any handedness bias that might be induced by interactions between the chiral bacteria and the upper and lower surfaces of the chamber. Plotting a histogram of the time-averaged spins across all experiments shows no discernible bias towards either vorticity handedness (Supplementary Fig. 1a), so this assumption is justified.

1.2 Statistical steady state

When estimating parameters using movies taken after 4 and 8 minutes with equal weight, we are assuming that the suspension has reached a sufficiently statistically-steady state no later than 4 minutes after injection. We checked this assumption by comparing the spin–spin correlation in movies taken at 4 and 8 minutes with identically acquired movies taken 1 minute after injection. We found that the mean correlation changed much less between 4 and 8 minutes than between 1 and 4 minutes for experiments both below and above the critical transition gap size (Supplementary Fig. 1b), indicating sufficient equilibration to perform parameter estimation at both 4 and 8 minutes independently.

1.3 Phase-space exploration

A system following an equilibrium-like description such as the model in Eqs. (2) and (3) will not be frozen into one configuration for all time. Rather, given sufficient time, it should explore all states of its configuration space according to a steady-state probability distribution. Our experiments show this exploration behaviour, with spins fluctuating and changing sign over time (Supplementary Fig. 1e,f). This is particularly noticeable when comparing between the same experiment at the two observation times of 4 and 8 minutes, during which time some (Supplementary Fig. 1c) or most (Supplementary Fig. 1d) spins may have changed orientation. However, the system is always exploring a distribution consistent with a particular preferred antiferromagnetic or ferromagnetic correlation, dependent on the gap size.

DOI: 10.1038/NPHYS3607

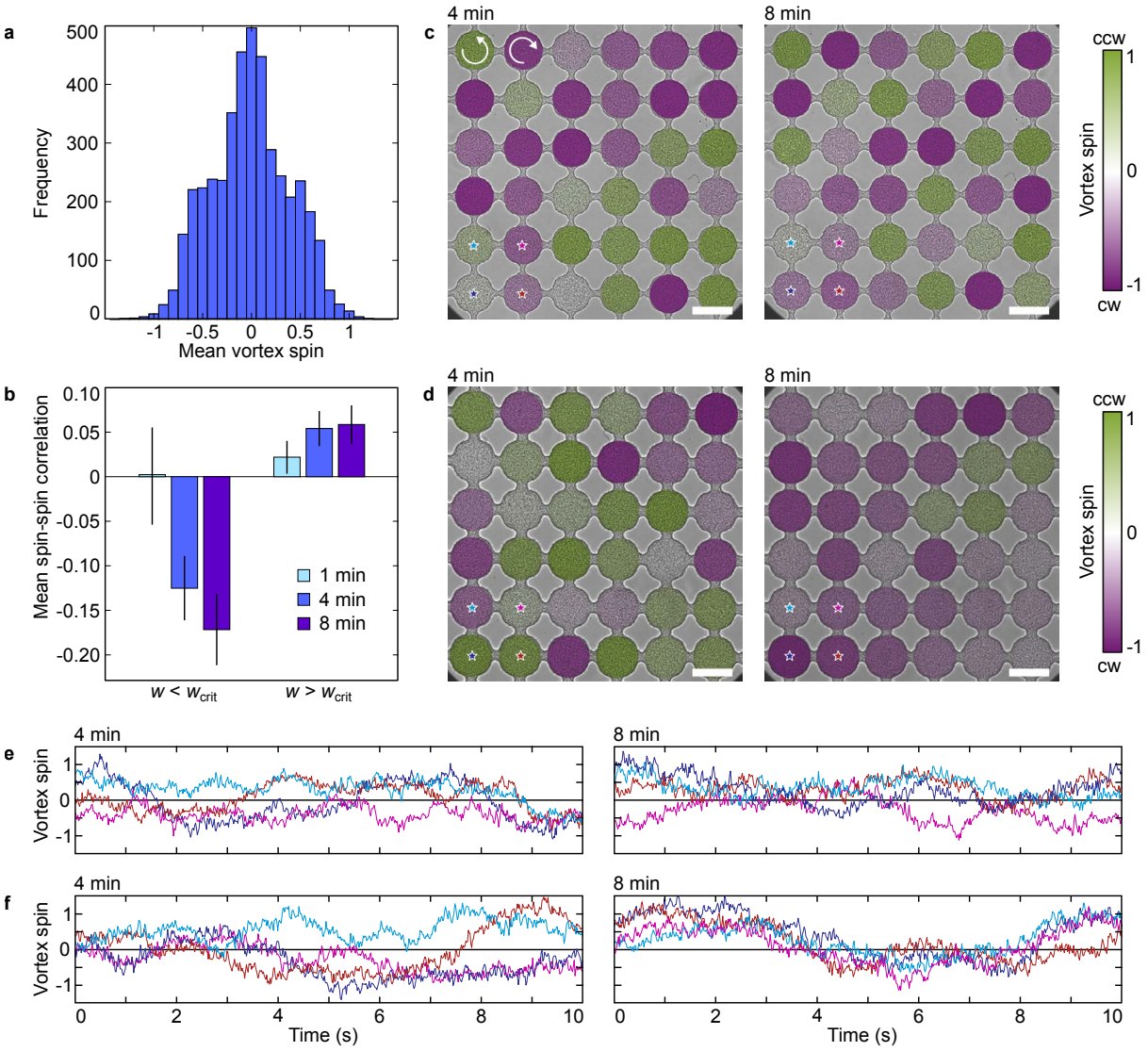

Supplementary Figure 1 – Experiments are unbiased and explore a statistical steady state. a, Histogram of time-averaged vortex spin of each cavity $\langle V_i(t)\rangle$ across all square lattice experiments, exhibiting symmetry about zero spin. **b**, Spin–spin correlation χ averaged over all movies taken 1, 4 or 8 min after injection, categorised by gap size $w < w_{\mathrm{crit}}$ or $w > w_{\mathrm{crit}}$. The suspension is not equilibrated 1 min after injection, but results are similar between 4 and 8 min indicating equilibration. **c,d**, Frames from movies taken from two experiments at 4 and 8 min, with $w = 7\,\mu$m (**c**) and $w = 11\,\mu$m (**d**), showing phase-space exploration between the observation times. **e,f**, Spin–time traces of four adjacent vortices from the experiments shown in **c,d** (line colours correspond to star colours in **c,d**).

2 Parameter inference under the full model

For a given sequence of discrete experimental observations $\{\mathbf{V}(t), \mathbf{P}(t)\}_{t=n\Delta t}$ derived from one movie with constant time step $\Delta t = 1/60$ s and rescaled by $\overline{U}$ (Methods), we wish to estimate the most likely parameter values assuming the SDE model in Eqs. (2) and (3) holds. We do this by first discretizing Eqs. (2) and (3) and then applying linear regression. First, the rescaling by $\overline{U}$ used to eliminate variable oxygenation effects (Methods) implies that we must also rescale the time step to $\delta t = \Delta t/\tau$, where $\tau = \ell/\overline{U}$ is a time scaling with length scale $\ell = 1\,\mu$m selected as the characteristic width of a bacterium. All parameters are subsequently dimensionless under these scalings; those for an *unscaled* experiment (denoted by tildes) with desired or observed RMS velocity $\overline{U}$ can then be recovered as $\tilde{J}_v = J_v/\tau$, $\tilde{J}_p = J_p/\tau$, $\tilde{a}_v = a_v/\tau$, $\tilde{b}_v = b_v/(\overline{U}^2\tau)$, $\tilde{a}_p = a_p/\tau$, $\tilde{T}_v = \overline{U}^2 T_v/\tau$ and $\tilde{T}_p = \overline{U}^2 T_p/\tau$. Now, using this

time step, Eqs. (2) and (3) discretize in the Euler–Maruyama scheme[1] as

$$\mathbf{V}(t+\delta t) = \mathbf{V}(t) - (\partial H/\partial \mathbf{V})_t \delta t + \sqrt{2T_v \delta t}\mathbf{N}_v, \tag{S1}$$

$$\mathbf{P}(t+\delta t) = \mathbf{P}(t) - (\partial H/\partial \mathbf{P})_t \delta t + \sqrt{2T_p \delta t}\mathbf{N}_p, \tag{S2}$$

where $\mathbf{N}_v$ and $\mathbf{N}_p$ are vectors of independent $\mathcal{N}(0,1)$ random variables. Component-wise, Eqs. (S1) and (S2) read

$$V_i(t+\delta t) = (1-a_v\delta t)V_i(t) - b_v\delta t V_i(t)^3 + J_v\delta t \sum_{j\,:\,V_j\sim V_i} V_j(t) + J_p\delta t \sum_{j\,:\,P_j\sim V_i} P_j(t) + \sqrt{2T_v\delta t}N_{v,i}, \tag{S3}$$

$$P_i(t+\delta t) = (1-a_p\delta t)P_i(t) + J_p\delta t \sum_{j\,:\,V_j\sim P_i} V_j(t) + \sqrt{2T_p\delta t}N_{p,i}. \tag{S4}$$

By Eq. (S4), using data from all observation times and vortices to perform a linear regression of $P_i(t+\delta t)$ on the two variables

$$\left\{ P_i(t), \sum_{j\,:\,V_j\sim P_i} V_j(t) \right\}$$

yields estimates $\{1-\hat{a}_p\delta t, \hat{J}_p\delta t\}$ of the variables' respective coefficients and thence estimates $\hat{a}_p$ and $\hat{J}_p$ of a_p and J_p. Next, after substituting the estimate $J_p = \hat{J}_p$ into Eq. (S3) to reduce the dimensionality, a linear regression of $V_i(t+\delta t) - \hat{J}_p\delta t \sum_{j\,:\,P_j\sim V_i} P_j(t)$ on the three variables

$$\left\{ V_i(t), V_i(t)^3, \sum_{j\,:\,V_j\sim V_i} V_j(t) \right\}$$

yields estimates $\{1-\hat{a}_v\delta t, -\hat{b}_v\delta t, \hat{J}_v\delta t\}$ of their respective coefficients and thence estimates $\hat{a}_v$, $\hat{b}_v$ and $\hat{J}_v$ of a_v, b_v and J_v. Finally, the variances $2\hat{T}_v\delta t$ and $2\hat{T}_p\delta t$ of the residuals to the regressions in Eqs. (S3) and (S4) respectively yield estimates $\hat{T}_v$ and $\hat{T}_p$ of T_v and T_p.

Boundary terms are treated by assuming a truly finite system with free boundary conditions, effectively fixing all pillar and vortex spins at zero outside of the observed domain. Since we do not image a full 6×6 offset lattice of pillars, but instead the internal 5×5 lattice, periodic boundary conditions are not possible; indeed, for a small system, free boundaries are often preferable over periodic boundaries in general.

3 Simulations

To reconstruct the vortex–vortex correlation function $\chi(w)$ as a continuous function of gap width w, we reconstructed the parameters as functions of w from the experimental data and numerically integrated the model in Eqs. (2) and (3) over a range of w. The simulations can then be used to explore the system on longer time scales than possible experimentally. We discuss this process further in the following section.

3.1 Parameter reconstruction

Running the parameter estimation procedure for every suitable experimental movie (those not containing any 'locked' immobile cavities, occasionally seen at small w) results in a set of parameter estimates $\mathcal{E}_i$ at gaps w_i. Estimates for movies from the same experiment were averaged, and then placed into non-overlapping w-bins of size 2.5 μm and averaged in both w and parameter value within each bin (Supplementary Fig. 2, points). Using non-linear least-squares regression estimation, the parameters were then

DOI: 10.1038/NPHYS3607

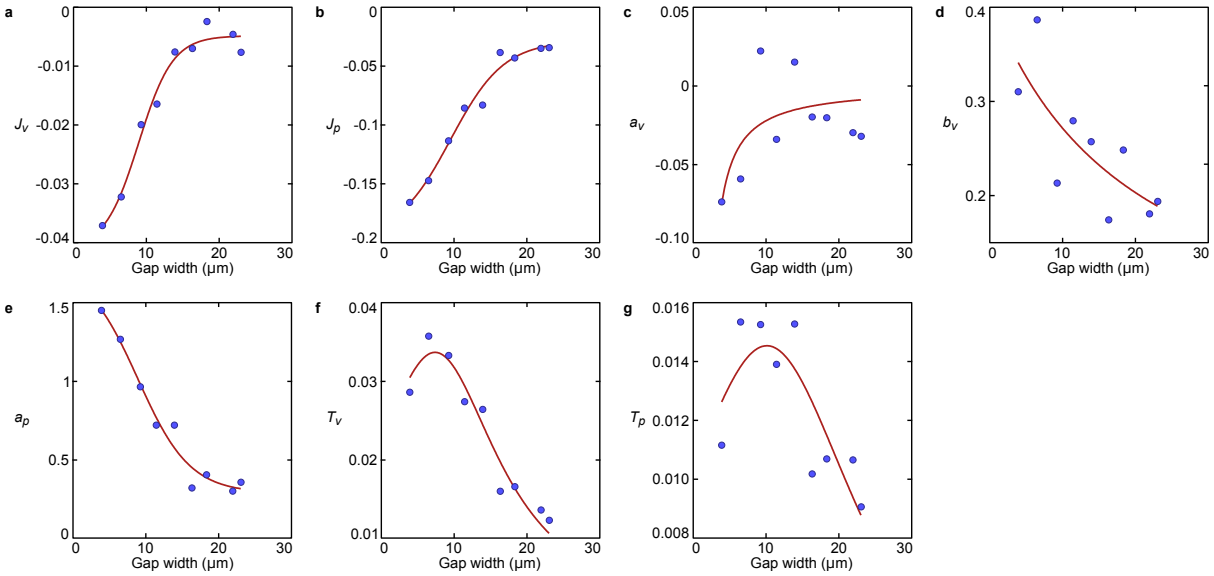

Supplementary Figure 2 – Parameters in the full model can be inferred using regression methods. Points are averages within non-overlapping $2.5\,\mu$m bins of parameters inferred for each experiment using linear regression on a discretization of Eqs. (2) and (3), and lines are parametric best fits of selected functional forms to the points (Sec. 2).

fitted with chosen functional forms: J_v, J_p, a_p with a logistic function $\alpha_1 + \alpha_2/(1+10^{\alpha_3(\alpha_4-w)})$; a_v, b_v with a rational function $\alpha_1/(w+\alpha_2)$; and T_v, T_p with a rational function $(\alpha_1+\alpha_2 w)/(w^2+\alpha_3 w+\alpha_4)$ (Supplementary Fig. 2, lines). These forms were chosen as appearing to give the best representation of the data points' behaviour (such as not introducing maxima where none are observed for J_v, J_p, a_p, and not presuming too detailed a functional form for the noisiest parameters a_v and b_v) with the fewest possible fit parameters.

3.2 Simulation method

We numerically integrated Eqs. (2) and (3) using the discretization in Eqs. (S1) and (S2), wherein we set $N = 6$ and $\delta t = 1/600$ (equivalent to $1/60\,$s when $\overline{U} = 10\,\mu$m). We initialized $\mathbf{V}$ and $\mathbf{P}$ to zero, and after an equilibration period of $50/\delta t$ frames we recorded every frame. Trial and error showed an observation period of $8000/\delta t$ frames in an ensemble of 25 identical repetitions to be sufficient to obtain a stable estimate of the average vortex–vortex correlation χ. This was evaluated at each of 101 regularly-spaced values of w in the range $\min w_i \leq w \leq \max w_i$ (Fig. 1j).

In all simulations we use free boundary conditions (that is, setting components of $\mathbf{P}$ and $\mathbf{V}$ to zero outside of the simulation domain) consistent with the conditions used in parameter inference. Because of the small size of the system being simulated, periodic boundary conditions are inappropriate as they have too great a dynamical influence and do not reproduce the expected spin–spin correlation behaviour. Simulations on moderately larger lattices with free boundary conditions retain the same form of correlation curve as for the 6×6 grid, but as the number of grid points increases, the antiferromagnetic phase eventually disappears. This reflects the sensitivity of the system to fluctuations as vortex and pillar interactions compete near to a critical point; were experiments to be performed on larger lattices and parameters inferred from that data, this regime would reappear in simulations.

3.3 Spin fluctuations

As in the experiments, after equilibrating during the burn-in period, each simulation explores configuration space within the statistical steady state. The simulations then allow us to examine system behaviour over time scales longer than those of the experimental movies, whose durations were constrained by

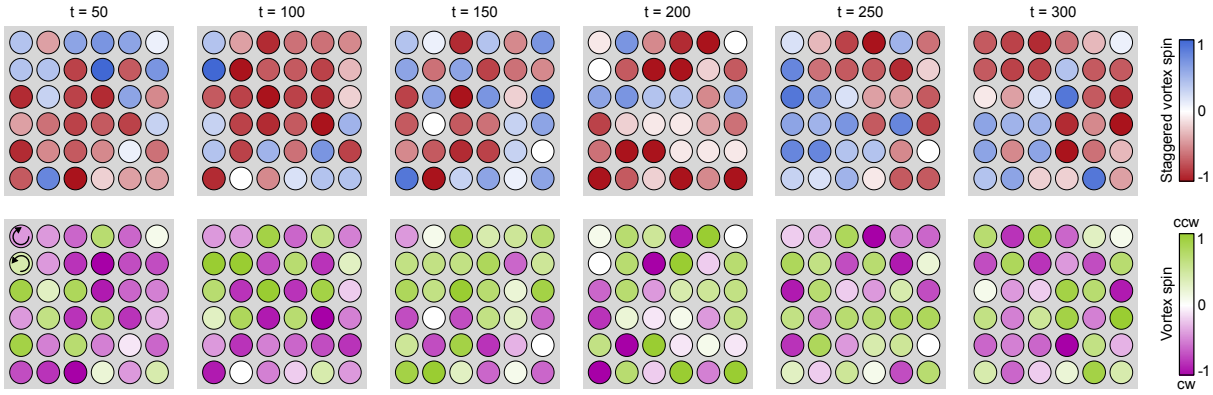

Supplementary Figure 3 – Simulations of the full model reproduce the spin-flip dynamics over long times. Frames of a simulation using parameter values at $w = 4\,\mu$m from the reconstructions in Supplementary Fig. 2. Top row: staggered vortex spins, corresponding to multiplying each spin site alternately by ± 1 to show coherent antiferromagnetic domains as single colours. Bottom row: unstaggered vortex spins. Domain fluctuations and large-scale spin flips can be seen over the simulation at times extending to an equivalent of double or triple the lengths of typical observations.

equipment data capacity. In particular, the simulations exhibit domain fluctuations and spin flipping as observed in the experiments (Supplementary Fig. 1c–f), while better demonstrating the system fully exploring configuration space. Supplementary Fig. 3 depicts a simulation using reconstructed parameter values at $w = 4\,\mu$m, firmly inside the antiferromagnetic regime, run for a length equivalent to approximately 25 s of an experiment with RMS kinetic energy $\bar{U} = 12\,\mu\text{ms}^{-1}$ (the average seen in experiments; see Methods), exhibiting dynamic configuration exploration within an equilibrium distribution favouring antiferromagnetic correlation.

4 Reduction to vortex-only model

A true Langevin equation for $\mathbf{V}$ can be obtained by integrating Eq. (3) for $\mathbf{P}$ as a function of $\mathbf{V}$ and back-substituting[2,3]. Since Eq. (3) is linear in $\mathbf{P}$, we have

$$P_i(t) = P_i(0)e^{-a_p t} + J_p \sum_{j:V_j \sim P_i} \int_0^t V_j(s) e^{a_p(s-t)}\, ds + \sqrt{2T_p} \int_0^t e^{a_p(s-t)}\, dW(s),$$

where the third term is an integral with respect to the standard Brownian motion $W(t)$. When $a_p t \gg 1$, the first term decays and the second can be approximated by pulling out $V_j(s)$ at $s = t$ (provided $\mathbf{V}$ varies sufficiently slowly over short time intervals), giving

$$P_i(t) \approx \frac{J_p}{a_p} \sum_{j:V_j \sim P_i} V_j(t) + \sqrt{2T_p} \int_0^t e^{a_p(s-t)}\, dW(s). \tag{S5}$$

This is valid here since $a_p \sim 1$ (Supplementary Fig. 2) and each 10 s experimental movie reaches non-dimensional times $t = (10\,\text{s})/\tau \sim 100$. Thus P_i reduces to time-autocorrelated noise $\nu(t) = \sqrt{2T_p}\int_0^t e^{a_p(s-t)}\, dW(s)$ about a mean proportional to the average spin of adjacent vortices $[P_i]_V = \frac{1}{4}\sum_{j:V_j \sim P_i} V_j$; that is, $P_i \approx (4J_p/a_p)[P_i]_V + \nu$. The noise has autocorrelation

$$C(t,t') = \mathbb{E}\left[\nu(t)\nu(t')\right] = \frac{T_p}{a_p}\left[e^{-a_p|t-t'|} - e^{-a_p(t+t')}\right] \approx \frac{T_p}{a_p} e^{-a_p|t-t'|}$$

for $a_p t, a_p t' \gg 1$. In this limit, C decays rapidly away from $t = t'$, and $\nu(t)$ is approximately normally distributed at every t with variance T_p/a_p.

DOI: 10.1038/NPHYS3607

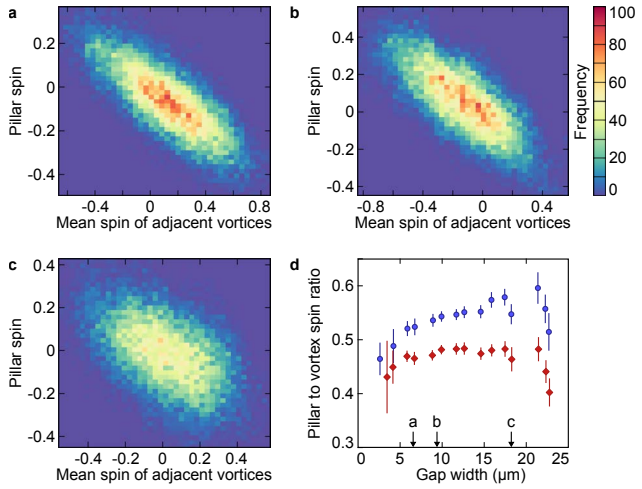

Supplementary Figure 4 – Pillar spin distributions vary linearly with the average spin of adjacent vortices. **a–c**, Two-dimensional histogram of $(P_i, [P_i]_V)$ from three example movies, showing uniform spread about a line $P_i \propto [P_i]_V$. Gap widths 7, 10 and 18 μm, respectively. **d**, The proportionality constant α, where $P_i \approx -\alpha[P_i]_V$, depends weakly on gap width. Direct correlations from data (blue circles) compare well with the theoretical result $\alpha = -4J_p/a_p$ calculated with inferred model parameters (red diamonds). Each point represents an average over ≥ 5 movies in 3 μm bins at 1.5 μm intervals; vertical bars indicate standard errors (Methods).

Now, in Eq. (2), interaction with $\mathbf{P}$ arises through the term $J_p \sum_{j:P_j \sim V_i} P_j$ in $\partial H/\partial V_i$. By Eq. (S5), this approximates to

$$J_p \sum_{j:P_j \sim V_i} P_j \approx \frac{J_p^2}{a_p} \left[4V_i + 2 \sum_{j:V_j \sim V_i} V_j + (\text{n.n.n.}) \right] + J_p \sum_{j=1}^{4} \nu^{(j)}, \tag{S6}$$

where $\nu^{(j)}$ are i.i.d. noise processes as above, and 'n.n.n.' denotes next-nearest-neighbour interactions which we neglect. When substituted into Eq. (2), each noise term contributes $J_p \nu^{(j)} dt$, which represents a contribution of the form $J_p \int_0^t \nu^{(j)}(s)\, ds$ in the formal integral representation of Eq. (2). Inserting the definition of ν into this integral and exchanging the order of integration implies

$$J_p \int_0^t \nu^{(j)}(s)\, ds = \frac{J_p \sqrt{2T_p}}{a_p} \int_0^t [1 - e^{a_p(s-t)}]\, dW(s).$$

In our experiments, we found $|J_p/a_p| \approx 1/10$ and $T_p \lesssim T_v$ over all gap widths (Supplementary Fig. 2), so these are weak contributions to the noise in $\mathbf{V}$. Indeed, the integral has variance $t - 3/(2a_p) + O(e^{-a_p t})$ as $t \to \infty$, so for large a_p its effect can be approximated by the pure Brownian motion $\int_0^t dW(r)$ (whose variance is t). Thus the contributions $J_p \nu^{(j)} dt$ reduce to small Brownian noise terms $(J_p \sqrt{2T_p}/a_p) dW$, which combine with the existing noise into one single term $\sqrt{2T} dW$ of slightly increased temperature $T = T_v + 4T_p J_p^2/a_p^2$. Substituting Eq. (S6) into Eq. (2) yields new approximate $\mathbf{V}$ dynamics obeying $d\mathbf{V} = -(\partial \hat{H}/\partial \mathbf{V})dt + \sqrt{2T} d\mathbf{W}$ with effective Hamiltonian

$$\hat{H}(\mathbf{V}) = -J \sum_{V_i \sim V_j} V_i V_j + \sum_{V_i} \left(\tfrac{1}{2} a V_i^2 + \tfrac{1}{4} b V_i^4 \right),$$

where the effective coupling constants are $J = J_v + 2J_p^2/a_p$, $a = a_v - 4J_p^2/a_p$ and $b = b_v$.

Though this reduction will only be achieved exactly in the thermodynamic limit when boundary effects are eliminated, this still serves as a good approximation for a finite system. To verify this reduction with our experimental data, we compared P_i with $[P_i]_V$. Consistent with Eq. (S5), we found P_i to be linearly correlated with $[P_i]_V$ in every square-lattice experiment (Supplementary Fig. 4a–c), confirming our use of a quadratic potential for $\mathbf{P}$. Writing $-\alpha$ for the correlation coefficient, we found $\alpha \approx 0.5$ with weak dependence on the gap width; this compares well with the analytic result $\alpha = -4J_p/a_p$ from Eq. (S5) when calculated using experimentally inferred parameters (Supplementary Fig. 4d).

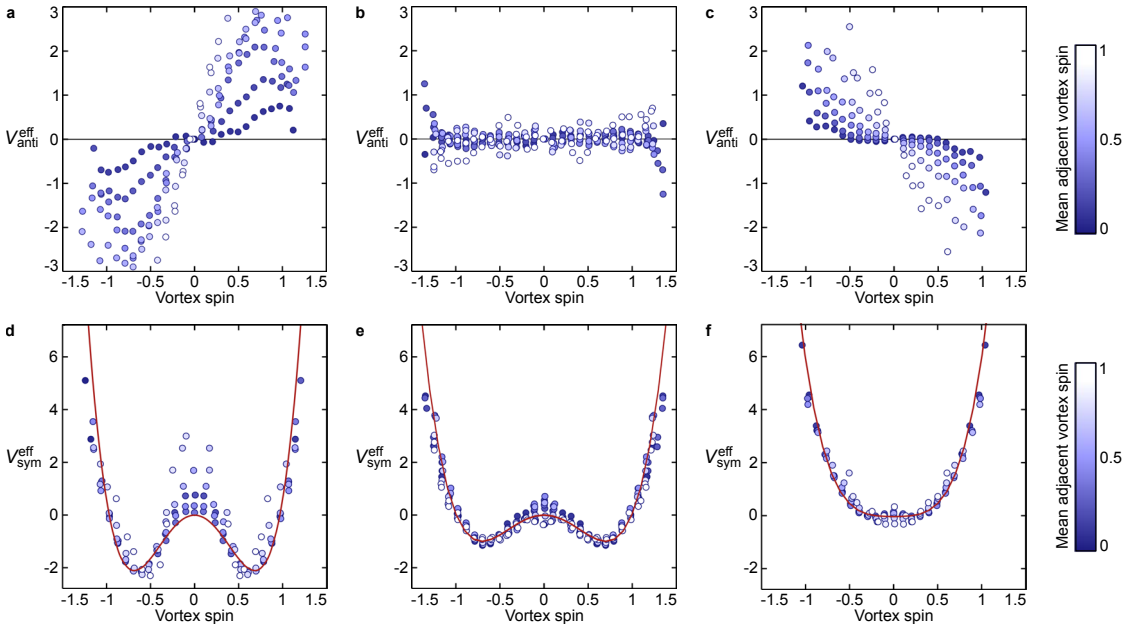

Supplementary Figure 5 – Parameters in the reduced model can be inferred by fitting effective single-spin potentials. Reduced model parameters βJ, βa and βb are estimated by fitting the antisymmetric and symmetric parts of the effective potential $\mathcal{V}^{\mathrm{eff}}(V_i \,|\, [V_i]_V)$ (Sec. 5.1). Data shown from three example movies of square lattices with gap widths $7\,\mu$m (**a,d**), $10\,\mu$m (**b,e**) and $18\,\mu$m (**c,f**). **a–c**, The antisymmetric part of the effective potential reveals the vortex–vortex coupling βJ, spanning the range $J < 0$ (**a**), $J \approx 0$ (**b**) and $J > 0$ (**c**). Estimated $\mathcal{V}^{\mathrm{eff}}_{\mathrm{anti}}$ (points), coloured by mean adjacent spin $[V_i]_V$. **d–f**, The symmetric part of the effective potential reveals the non-interacting single-spin potential, which flattens with increasing gap width. Estimated $\mathcal{V}^{\mathrm{eff}}_{\mathrm{sym}}$ (points) coloured by mean adjacent spin $[V_i]_V$, with fitted single-spin potentials (lines).

5 Parameter inference under the reduced model

5.1 Distribution fitting

We assume that $\mathbf{V}$ obeys a Boltzmann distribution $p(\mathbf{V}) \propto e^{-\beta \hat{H}(\mathbf{V})}$. The probability density $p(V_i \,|\, [V_i]_V)$ of one spin V_i conditional on the mean of its adjacent spins $[V_i]_V = \frac{1}{4}\sum_{j\,:\,V_j \sim V_i} V_j$ satisfies

$$\log p(V_i \,|\, [V_i]_V) - \log p(0 \,|\, [V_i]_V) = -\mathcal{V}^{\mathrm{eff}}(V_i \,|\, [V_i]_V), \tag{S7}$$

where we have defined the effective single-vortex potential

$$\mathcal{V}^{\mathrm{eff}}(V_i \,|\, [V_i]_V) = -4\beta J V_i [V_i]_V + \tfrac{1}{2}\beta a V_i^2 + \tfrac{1}{4}\beta b V_i^4.$$

We estimate $p(V_i \,|\, [V_i]_V)$ for each movie by forming a two-dimensional histogram in V_i and $[V_i]_V$ and then normalizing at every fixed V_i. In forming the histogram, we exploit the invariance of $\mathcal{V}^{\mathrm{eff}}$ under the transformation $V_i \to -V_i$ and $[V_i]_V \to -[V_i]_V$ to double the number of data points.

Taking the antisymmetric part $\mathcal{V}^{\mathrm{eff}}_{\mathrm{anti}} = \frac{1}{2}\left[\mathcal{V}^{\mathrm{eff}}(V_i \,|\, [V_i]_V) - \mathcal{V}^{\mathrm{eff}}(-V_i \,|\, [V_i]_V)\right]$ eliminates the non-interacting terms, so Eq. (S7) implies

$$\tfrac{1}{2}\left[-\log p(V_i \,|\, [V_i]_V) + \log p(-V_i \,|\, [V_i]_V)\right] = -4\beta J V_i [V_i]_V.$$

This allows estimation of the interaction constant βJ from the density $p(V_i|[V_i]_V)$ (Fig. 2a and Supplementary Fig. 5a–c). The symmetric part $\mathcal{V}^{\mathrm{eff}}_{\mathrm{sym}} = \frac{1}{2}\left[\mathcal{V}^{\mathrm{eff}}(V_i \,|\, [V_i]_V) + \mathcal{V}^{\mathrm{eff}}(-V_i \,|\, [V_i]_V)\right]$ eliminates the interaction term in a similar fashion, so Eq. (S7) now implies

$$\frac{1}{2}\left[-\log p(V_i \,|\, [V_i]_V) - \log p(-V_i \,|\, [V_i]_V)\right] + \log p(0 \,|\, [V_i]_V) = \frac{1}{2}\beta a V_i^2 + \frac{1}{4}\beta b V_i^4.$$

DOI: 10.1038/NPHYS3607

Typically there are fewer observations near $V_i = 0$, so $p(0 \mid [V_i]_V)$ can be difficult to infer directly. Instead, we adjust $\log p(0 \mid [V_i]_V)$ for each $[V_i]_V$ bin to minimize the difference between $\mathcal{V}^{\text{eff}}_{\text{sym}}(V \mid [V_i]_V)$ and $\mathcal{V}^{\text{eff}}_{\text{sym}}(V \mid 0)$. We then fit the remaining single vortex potential with parameters βa and βb (Supplementary Fig. 5d–f), from which we compute the spins $\pm V_{\text{min}}$ ($V_{\text{min}} > 0$) minimizing the local effective single-spin energy $\mathcal{V}^{\text{eff}}_{\text{sym}}$, namely

$$V_{\text{min}} = \begin{cases} \sqrt{|a|/b} & \text{if } a < 0, \\ 0 & \text{if } a > 0, \end{cases}$$

and the effective spin-flip energy barrier

$$\mathcal{V}^{\text{eff}}_{\text{sym}}(0) - \mathcal{V}^{\text{eff}}_{\text{sym}}(\pm V_{\text{min}}) = \begin{cases} \beta a^2/(4b) & \text{if } a < 0, \\ 0 & \text{if } a > 0, \end{cases}$$

which together characterize the single-spin symmetric quartic potential (Fig. 2b,c).

To ensure boundary conditions do not have a strong effect on the inferred parameters by comparison with those used in the SDE discretization method (see below), boundary terms are treated in this method using neighbour averaging whereby the mean adjacent spin $[V_i]_V$ is computed as an average over only two spins (in a corner) or three spins (at an edge). This corresponds to assuming that, in each computation of $[V_i]_V$, spin sites absent from the lattice are the mean of the sites present in the sum.

5.2 SDE discretization

Estimations made by the above method were verified by estimations obtained through the same SDE discretization method used in the full model. Though the absence of pillars now means periodic boundary conditions could be used, we retain the free boundary conditions to maintain consistency with the full model and for comparison with the averaging conditions used above. The components of the reduced model SDE $d\mathbf{V} = -(\partial \hat{H}/\partial \mathbf{V})dt + \sqrt{2T}d\mathbf{W}$ have Euler–Maruyama discretization

$$V_i(t+\delta t) = (1 - a\delta t)V_i(t) - b\delta t V_i(t)^3 + J\delta t \sum_{j\,:\,V_j \sim V_i} V_j(t) + \sqrt{2T\delta t}N_i,$$

where N_i are independent $\mathcal{N}(0,1)$ random variables. Performing linear regression of $V_i(t+\delta t)$ on the three variables

$$\left\{ V_i(t), V_i(t)^3, \sum_{j\,:\,V_j \sim V_i} V_j(t) \right\}$$

then gives estimates $\{1 - \hat{a}\delta t, -\hat{b}\delta t, \hat{J}\delta t\}$ of the respective coefficients, from which estimates $\hat{a}$, $\hat{b}$ and $\hat{J}$ of the variables a, b and J can be deduced. The estimate $\hat{T}$ of the fluctuation strength T is estimated via the variance $2\hat{T}\delta t$ of the residuals to the regression, which gives an estimate $\hat{\beta} = 1/\hat{T}$ of the inverse 'temperature' β in the Boltzmann distribution. The non-dimensional combinations $\hat{\beta}\hat{J}$, $\hat{\beta}\hat{a}$ and $\hat{\beta}\hat{b}$ can then be directly compared with the estimates obtained using the distribution-fitting method.

Though SDE discretization independently gives both temperature and coupling constants, it is likely to possess greater intrinsic bias than distribution fitting. Discretization was the only method open for the full model, as the SDE steady state cannot be solved analytically. However, since the reduced model allows for distribution fitting, coupling constant values obtained using that method are preferable, with SDE discretization functioning as an independent verification.

6 One-dimensional geometries

As well as the square and triangular lattices discussed in the main text (Figs. 1 and 3), we also performed experiments on lines of connected vortices (Supplementary Fig. 6). As the finite-circumference

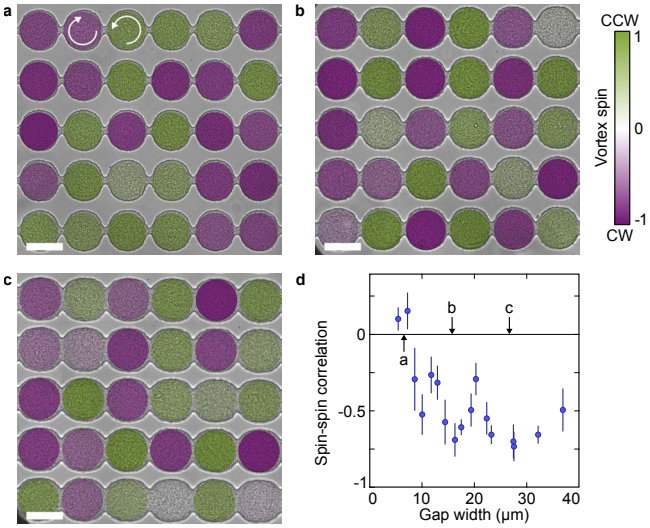

Supplementary Figure 6 – One-dimensional lattices adopt antiferromagnetic states. **a**, At the smallest gap widths, vortices interact weakly resulting in strong but randomly oriented circulation. Gap width 7 μm. **b**,**c**, Intermediate and large gaps show strong antiferromagnetic order. Gap widths 16 and 28 μm. False colour in **a**–**c** denotes measured vortex spin. Scale bar: 50 μm. **d**, The spin–spin correlation χ shows the antiferromagnetic state to be largely favoured in lines of cavities. Each point represents an average over ≥ 5 movies in 3 μm bins at 1.5 μm intervals; vertical bars indicate standard errors (Methods).

pillars are no longer present in a line of vortices, it is not clear whether the same edge-current-mediated ferromagnetism should be expected. Indeed, we did not observe significant ferromagnetic behaviour at any gap sizes (Supplementary Fig. 6d), suggesting that it is difficult to maintain the single long, uniform edge current that would be necessary for a positively-correlated state. Furthermore, experiments performed on isolated pairs of vortices support these results, in which 76% of the vortex pairs adopted an antiferromagnetic state (out of 34 pairs) with gap sizes between 20 μm and 38 μm.

7 Model generalizations

There are more general forms of the model in Eqs. (2) and (3) which preserve at least some form of local equilibrium. These add flexibility through further couplings or fields at the expense of increased complexity. Though we did not find a need for any further generality, they cannot necessarily be disregarded *a priori*, which we discuss further here.

7.1 Cross-coupled models with frictional dissipation

One generalization of Eqs. (2) and (3) is to add dissipative cross-couplings. Write $\mathbf{X} = (\mathbf{V}, \mathbf{P})$ for the concatenation of the vectors $\mathbf{V}$ and $\mathbf{P}$. In this formalism, Eqs. (2) and (3) read

$$dX_i = -\frac{\partial H}{\partial X_i}dt + \sqrt{2T_i}dW_i, \tag{S8}$$

where T_i is T_v or T_p as appropriate and the W_i are uncorrelated Wiener processes as before. (Repeated indices do not imply summation.) However, in general, we need not have diagonal coupling to derivatives of H. We could instead write[4]

$$dX_i = -\sum_j M_{ij}\frac{\partial H}{\partial X_j}dt + \sum_j m_{ij}\sqrt{2T_j}dW_j,$$

where the M_{ij} are the components of a more general coupling matrix, and $\mathbf{m}$ is the square-root matrix such that $\mathbf{m}^2 = \mathbf{M}$. Onsager reciprocity would then demand $M_{ij} = M_{ji}$ if the vortex spins and pillar flows were relaxing to a true thermodynamic equilibrium with $T_v = T_p$.

The simplest form of this generalization would be to posit a constant coupling between a vortex V_i and the gradients $\partial H/\partial P_j$ of its neighbouring pillars P_j, plus the corresponding reverse coupling. However, a single bacterial vortex experiences most frictional dissipation against the confining upper and lower walls of the cavity, rather than against the much smaller and more porous contact area of the edge currents. Similarly, a single pillar edge current experiences most friction against the solid

DOI: 10.1038/NPHYS3607

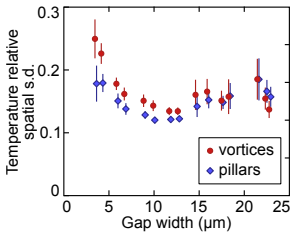

Supplementary Figure 7 – Vortices and pillars show low variability in their individual fluctuation strengths. Relative standard deviations ρ_v and ρ_p of per-site temperatures for vortices (red circles) and pillars (blue diamonds), as defined in the text, are small across gap sizes, only rising at the smallest gaps before the antiferromagnetic–ferromagnetic transition.

pillar walls rather than the porous vortex boundary. This implies that vortex–pillar frictional couplings through a non-diagonal matrix M_{ij} are small, and for this reason we have neglected them here. Indeed, including such couplings would add further parameters to fit in an already strongly fluctuating system, necessitating much more data to statistically distinguish these parameters from zero.

7.2 Spatially variable temperature

Another generalization would be to regard each vortex (and pillar) as possessing its own intrinsic temperature, introducing spatial dependence to the fluctuations. In this scenario, Eq. (S8) would still hold but with the vector of temperatures T_i now no longer constrained to be T_v or T_p. Since the random fluctuations are likely the result of microscopic cell–cell interactions, similar to Brownian motion, temperature variation would be driven by inhomogeneous initial conditions of the suspension, whereby differences in cell or oxygen concentration across the grid of chambers could induce some vortices to fluctuate with greater strength than others. These temperature inhomogeneities may then equilibrate on a time scale beyond that of the experiments due to poor inter-cavity mixing of cells, particularly at the smallest gap sizes. However, provided the fluctuations are zero-mean, inhomogeneous vortex and pillar temperatures should not have a strong effect on the parameters inferred by the linear regression method described in Section 2.

To gauge the extent of any such inhomogeneities, we computed the per-site fluctuation strength T_i as the variance of the residuals to the regression fit for each individual vortex or pillar i. We then computed the relative spatial standard deviations ρ_v and ρ_p for vortices and pillars as $\rho_{\{v,p\}} = \sqrt{\mathrm{Var}_{\{v,p\}}\, T_i}/T_{\{v,p\}}$, where T_v and T_p are the overall vortex temperatures as in Section 2. This gives a measure of spatial variability suitable for comparison between experiments. For most gap sizes, ρ_v and ρ_p averaged between 0.1 and 0.2, with ρ_v only rising above 0.2 at the smallest gap sizes before the antiferromagnetic–ferromagnetic transition (Supplementary Fig. 7). This suggests that the bulk of any variability is indeed driven by inhomogeneous initial conditions which do not dissipate quickly at small gap sizes. Though these values do indicate non-trivial spatial variability, they are not great enough to warrant detailed inclusion into our model as they would likely not have a great impact on the transition dynamics observed in simulations.

References

[1] Higham, D. J. An algorithmic introduction to numerical simulation of stochastic differential equations. *SIAM Rev.* **43**, 525–546 (2001).

[2] Hänggi, P. Generalized Langevin equations: A useful tool for the perplexed modeller of nonequilibrium fluctuations? In Schimansky-Geier, L. & Pöschel, T. (eds.) *Stochastic Dynamics*, vol. 484 of *Lecture Notes in Physics*, 15–22 (Springer, Heidelberg, 1997).

[3] Dunkel, J. & Hänggi, P. Relativistic Brownian motion. *Phys. Rep.* **471**, 1–73 (2009).

[4] Español, P. Statistical mechanics of coarse-graining. In Karttunen, M., Lukkarinen, A. & Vattulainen, I. (eds.) *Novel Methods in Soft Matter Simulations*, vol. 640 of *Lecture Notes in Physics*, 69–115 (Springer, Heidelberg, 2004).